ADVANCED FUNCTIONAL MATERIALS
www.afm-journal.de

Materials Views
www.MaterialsViews.com

Shape-Memory Microfluidics

*Aditya Balasubramanian, Robert Morhard, and Christopher J Bettinger**

Materials with embedded vascular networks afford rapid and enhanced control over bulk material properties including thermoregulation and distribution of active compounds such as healing agents or stimuli. Vascularized materials have a wide range of potential applications in self-healing systems and tissue engineering constructs. Here, the application of vascularized materials for accelerated phase transitions in stimuli-responsive microfluidic networks is reported. Poly(ester amide) elastomers are hygroscopic and exhibit thermomechanical properties ($T_g \approx 37$ °C) that enable heating or hydration to be used as stimuli to induce glassy-rubbery transitions. Hydration-dependent elasticity serves as the basis for stimuli-responsive shape-memory microfluidic networks. Recovery kinetics in shape-memory microfluidics are measured under several operating modes. Perfusion-assisted delivery of stimulus to the bulk volume of shape-memory microfluidics dramatically accelerates shape recovery kinetics compared to devices that are not perfused. The recovery times are 4.2 ± 0.1 h and 8.0 ± 0.3 h in the perfused and non-perfused cases, respectively. The recovery kinetics of the shape-memory microfluidic devices operating in various modes of stimuli delivery can be accurately predicted through finite element simulations. This work demonstrates the utility of vascularized materials as a strategy to reduce the characteristic length scale for diffusion, thereby accelerating the actuation of stimuli-responsive bulk materials.

1. Introduction

Vascular networks play an integral role in the efficient transportation and distribution of fluids in plants and animals.[1] Large organisms such as mammals[2] and trees[3] maintain homeostasis, in part, by utilizing pervasive vascular networks in large structures (≈1 cm^3) to facilitate the following functions: 1) rapid supply of nutrients, removal of metabolic by-products, and distribution of bioactive molecules; 2) facilitate thermal regulation; and 3) supply of bioactive agents for wound healing and repair. The efficient mass transfer of native vascular networks can be recapitulated in synthetic materials (**Figure 1**).[4–9]

A. Balasubramanian, R. Morhard, Prof. C. J. Bettinger
Department of Biomedical Engineering
Department of Materials Science and Engineering
5000 Forbes Avenue, WEH 3325
Pittsburgh, PA 15213-3890, USA
E-mail: cbetting@andrew.cmu.edu
Prof. C. J. Bettinger
McGowan Institute of Regenerative Medicine
450 Technology Drive, Suite 300
Pittsburgh, PA 15219, USA

DOI: 10.1002/adfm.201203618

Biomimetic microvascular networks show great promise in the field of smart materials. For example, self-healing materials with embedded microfluidic networks can provide a continuous source of healing agents that can be distributed to the bulk volume very rapidly.[7]

Recent advances in micromachining and microfabrication have enabled the integration of artificial vascular networks composed of various natural and synthetic materials.[10–13] Vascular networks have been incorporated into tissue constructs in order to overcome mass transfer limitations.[14–16] Tissue engineering scaffolds with pre-fabricated microvascular networks can dramatically reduce the characteristic length scale for diffusion in bulk materials.[17–21] Vascularized scaffolds can accelerate nutrient supply and waste removal in highly metabolically active tissues such as the liver, heart, and kidney.[22–24] The maximum thickness of engineered tissue in the smallest dimension is ultimately limited by oxygen diffusion and is typically on the order of 150 μm.[25] Integrating vascular networks into scaffolds may permit an increase in the total volume of tissue constructs while maintaining a constant effective macroscopic diffusion length scale that permits adequate supply of nutrients.

Accelerated mass transfer in bulk materials afforded by embedded vascular structures may also expedite transitions in stimuli-responsive materials. For example, shape-memory polymers (SMPs)[26–28] typically depend on the distribution of a stimulus throughout the bulk in order to recover their permanent geometries. The time scales for phase transitions in thermo-responsive[29–31] and chemo-responsive SMPs[32–34] are governed by diffusion. Proof-of-concept materials are typically prepared into form factors with small effective diffusion length scales such as films or porous networks.[35] Such material geometries reduce the dimensions that govern the characteristic diffusion length scale and accelerate phase transitions. However, these form factors may have limited utility as bulk or structural materials in applications that require systems with uniformly large length scales. Here we report the design, fabrication, and operation of shape-memory microfluidic materials. We hypothesize that the rates of shape recovery in bulk chemo-responsive SMPs can be accelerated by reducing the effective macroscopic diffusion length scale by integrating synthetic vascular networks to rapidly distribute stimuli.

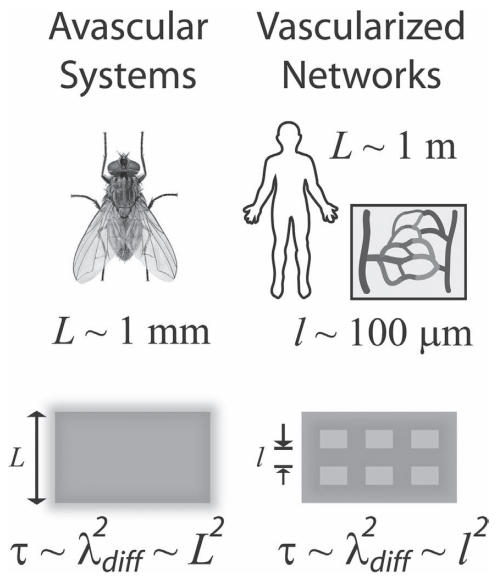

Figure 1. Vascularized networks enable the spatial scaling of biological matter while addressing potential diffusion limitations. A similar concept can be applied to vascularized smart materials. The effective macroscopic length scale for diffusion λ_{diff} in vascularized engineering materials is defined by the inter-channel spacing.

2. Results and Discussion

Poly(1,3-diamino-2-propanol-*co*-glycerol sebacate) (APS) was selected as the stimuli-responsive material for shape-memory microfluidics for several reasons. APS elastomers are a class of synthetic poly(ester amide)s that can be synthesized in large batches (≈100 g). APS elastomers are amenable to microfabrication techniques including replica-molding.[36] APS networks exhibit a glass transition temperature (T_g) in the range of 0 to 50 °C and are hygroscopic, yet exhibit limited dimensional swelling upon hydration. These properties enable glassy-rubbery transitions by either thermal activation or T_g depression upon hydration.[37]

Shape-memory microfluidics are fabricated through sequential replica-molding and lamination of microfabricated APS films (**Figure 2**). Thermal bonding of replica-molded APS films leads to covalent crosslinking of complementary functional groups at the interface, thereby producing vascular networks in high yields (**Figure 3**).[38] The vertical and horizontal microchannel spacing was chosen to be 350 and 240 μm in the *x*-*y* and *x*-*z* planes, respectively. Reducing the microchannel spacing below these critical values dramatically impacts the overall device yield.

Chemo-responsive shape-memory microfluidic devices fabricated from APS utilize water as the primary stimulus for shape recovery. Hydrated APS networks absorb up to 14 ± 2% (w/w) water with one-dimensional swelling $a = \frac{L}{L_0}$ of no more than 0.93 ± 0.1%. Hydrated APS networks likely sequester water within nanoporous domains, enabling water uptake in the absence of significant swelling. Fully hydrated and dehydrated APS networks exhibit T_g of –8.3 and 37 °C, respectively. The glassy-rubbery transition of APS upon hydration dictates the overall elastic modulus and the subsequent recovery of the permanent geometry.

A schematic for the operation of APS shape-memory microfluidic devices is shown in **Figure 4**. At temperatures $T > T_g$, APS networks exhibit a rubbery phase with a tensile Young's modulus of 4.58 ± 0.4 MPa (**Table 1**). Cooling the strained networks to $T < T_g$ programs the device into the temporary strained shape. The networks exhibit a glassy phase with a Young's modulus of 540 ± 30 MPa at temperatures $T < T_g$. Shape-memory APS microfluidic networks exhibit strain fixity ratios R_f of 95 ± 1%. R_f is defined as follows:

$$R_f = \frac{\varepsilon_u - \varepsilon_o}{\varepsilon_m - \varepsilon_o} \times 100 \quad (1)$$

In this expression, ε_m represents the deformation length immediately prior to unloading of the stress in the temporary state, ε_o is the original length of the device before deformation and ε_u is the deformation length of APS samples after removal of the applied stress.

The time-dependent recovery ratio $R_r(t)$ of shape-memory APS microfluidics in each of the three modes: 1) EXT_{stat}, where supply of water is from an external static bath, 2) INT_{perf}, where supply of water is internal through microfluidic channels, and 3) INT_{perf}+EXT_{stat}, where supply of water is from both an external bath and internal microfluidic channels (Supporting Information Figure S1), is plotted in **Figure 5**. The time-dependent recovery ratio $R_r(t)$ is defined as:

$$R_r(t) = \frac{\varepsilon_u(t) - \varepsilon_o}{\varepsilon_u - \varepsilon_o} \times 100 \quad (2)$$

where $\varepsilon_u(t)$ is the time-dependent deformation length of the device during hydration. The recovery can be described by considering two critical time points: 1) t_{onset} and 2) t_{50}. The time of strain recovery onset t_{onset} is defined as the time

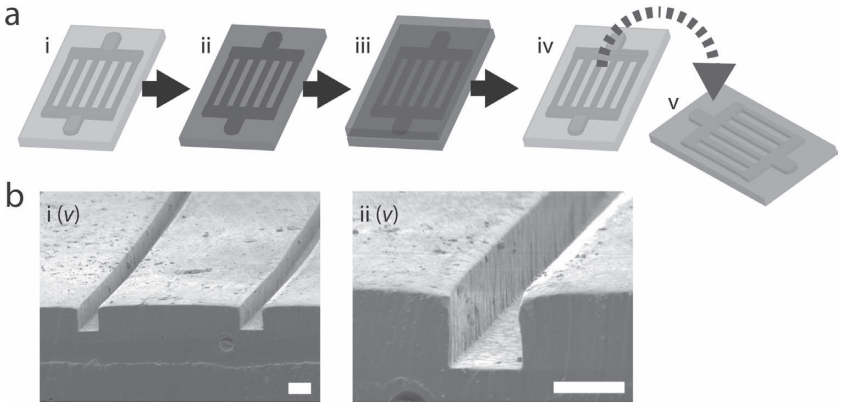

Figure 2. a) Schematic of APS micromolding process indicating i) silicon master, ii) silicon mold coated with sacrificial release layer, iii) APS pre-polymer spread on the mold, iv) silicon mold after dissolution of maltose and release of APS laminate and v) replica-molded APS laminate. b) Scanning electron microscopy images of micromolded APS laminates show surface patterns at i) low magnification and ii) high magnification. Scale bars represent 50 μm

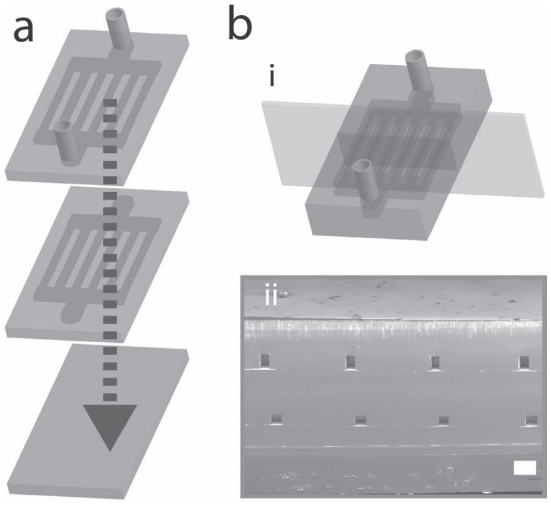

Figure 3. a) Multiple replica-molded APS networks are laminated and cured to produce the three-dimensional microfluidic network. b) i) A cross-sectional view of the device morphology yields insight into the integrity of the bonding. ii) A scanning electron microscopy image of this perspective indicates that the channels in the microfluidic network maintain their morphology and the lamination process is robust. Scale bar represents 100 μm.

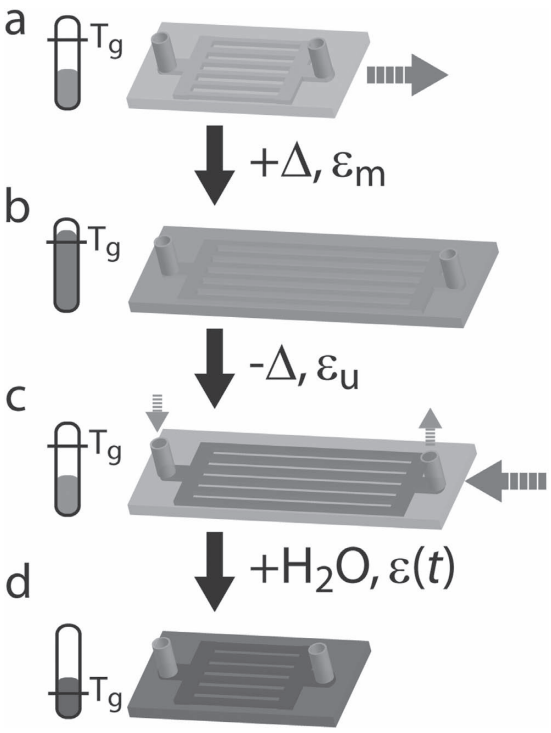

Figure 4. Schematic of APS microfluidic device operation. a) APS microfluidic networks are glassy at temperature $T < T_g$. b) The networks are then heated to $T > T_g$ and strained by the amount εm to yield the temporary shape in the rubbery phase. c) The networks are fixed into a temporary shape with a strain of εu after sequential recovery of the glassy phase upon cooling and removal of the deformation stress. At this point, the networks are hydrated in three pre-determined modes: 1) EXT_{stat}, 2) INT_{perf}, or 3) INT_{perf}+EXT_{stat}. d) The subsequent hydration of the network in all modes of operation leads to a reduction in the T_g. The gradual recovery of the rubbery phase initiates the recovery of the permanent geometry. The kinetics of this process are measured by measuring the time varying strain $\varepsilon_u(t)$, which in turn can be used to calculate the time-dependent recovery ratio $R_r(t)$. Schematic of APS microfluidic device fabrication.

required to achieve $R_r(t) = 95\%$ ($\varepsilon_{onset} = 0.95\varepsilon_u + 0.05\varepsilon_o$). The onset time represents the temporal lag between introduction of water into the vascular network and initiation of the shape recovery process of the APS networks. The parameter t_{50} is defined as time required to achieve a value of $R_r(t) = 50\%$ ($\varepsilon_{50} = 0.50\varepsilon_u + 0.50\varepsilon_o$). The values of t_{onset} and t_{50} are summarized in **Figure 6**. The experimental and predicted shape recovery kinetics were also compared by calculating the ratio of the definite integrals for $R_r(t)$ from the plots shown in Figure 5. The ratio of $\int R_r(t)_{exp}dt / \int R_r(t)_{mod}dt$ was calculated for 1) $EXT_{stat;}$ 2) INT_{perf}; and 3) $INT_{perf} + EXT_{stat}$, respectively as follows: 94.5%, 101%, 160%. The strain recovery kinetics are governed by the operation mode of stimulus delivery through the APS networks. Shape-memory microfluidic APS networks with perfusion-assisted delivery of stimuli possess a smaller effective macroscopic diffusion length scale and therefore a reduced time scale for actuation compared to networks that rely upon the external diffusion of stimulus alone.

There are several possible mechanisms for diffusion of plasticizers through glassy polymers: 1) Fickian diffusion;[39] 2) Case II[40,41] where penetration rate is determined by glassy-rubbery relaxation kinetics; and (3) Anomalous[42], a combination of Fickian diffusion and Case II transport. A generalized expression for diffusion of water into bulk APS networks can be written as follows:[43]

$$\tilde{M}_t = Kt^n \tag{3}$$

where $\tilde{M}_t$ is defined as $\tilde{M}_t = \frac{M_t}{M_\infty}$ where M_t is the mass fraction of water in APS networks at time t and M_∞ is the mass fraction of water in APS elastomers after complete hydration. The prefactor K represents a constant that incorporates network and penetrant charecteristics and n indicates the diffusional exponent. Fickian diffusion is consistent with $n = 0.5$ while anomolous behavour is represented by $0.5 < n < 1$. The nominalised sorbtion kinetics curves of water in APS at 20 °C and 30 °C are plotted in **Figure 7**. $\tilde{M}_t$ varies linearly with $t^{1/2}$ until late times indicating diffusion of water in APS follows Fickian behavour. The value of K is calculated to be 0.046 ± 0.002 min$^{-1/2}$ at 20 °C. Linear sorbtion kinetics beyond $\tilde{M}_t = 0.5$ indicate a strong dependence of the diffusion coeffecient of water in APS networks (D) with water concentration.[44],[45] This is presumably due to relaxation of glassy polymer networks and the increase in free volume upon hydration.[46] The dependence of D on local water concentration (c) is given by:

$$D(c) = D_o e^{\gamma c} \tag{4}$$

Table 1. Mechanical properties of dehydrated and hydrated APS.

APS	Modulus [Mpa]	UTS [MPa]	Elongation at break [%]
Dehydrated	540 ± 30	16.4 ± 1	6.06 ± 1
Hydrated	4.58 ± 0.4	0.619 ± 0.1	16.4 ± 3

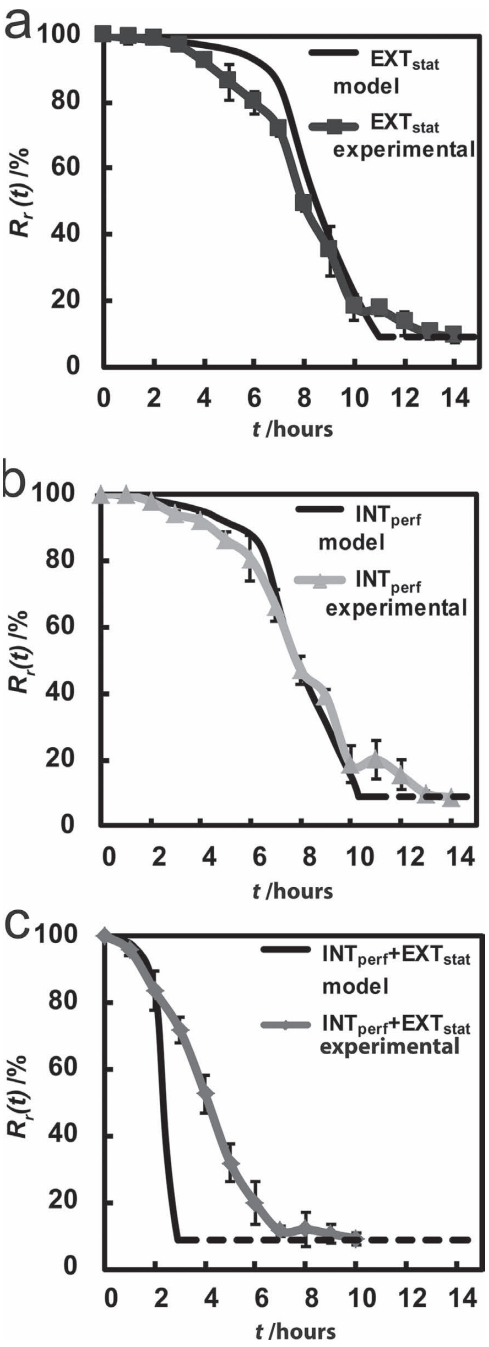

Figure 5. Comparison of simulated vs. experimental time-dependent strain recovery ratio $R_r(t)$ for the device operated in a) EXT_{stat} mode, b) INT_{perf} mode, and c) INT_{perf}+EXT_{stat} mode. The solid line indicates the recovery ratio predicted by finite element modeling. The dashed line indicates the maximum possible recovery ratio limit R_{rvy} due to swelling of the fully hydrated APS network. The absolute dimensional swelling of $\frac{L}{L_0} = 0.93 \pm 0.1\%$ corresponds to an $R_{rvy} = 91 \pm 1\%$.

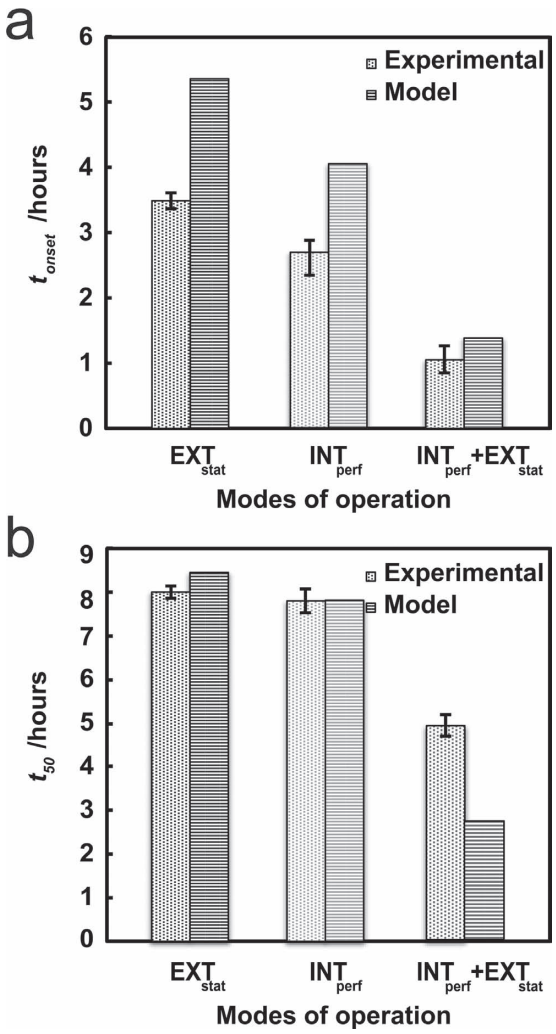

Figure 6. Experimental and predicted values for a) t_{onset} and b) t_{50} for shape-memory microfluidic APS devices.

where D_o is the limit diffusion coeffecient and γ is the plasticization coeffecient. The values of D_o and γ for water in APS are calculated to be 0.033×10^{-8} cm^2 s^{-1} and 0.54 cm^3 mmol^{-1}, respectively (Figure 7). The value of D_o is consistent with other amide containing polymers such as nylon6.[47] Inter-chain hydrogen bonding between amines and carbonyl groups in polyamides such as nylon6 and APS reduces free volume and decreases D_o. The calculated value of $\gamma_{APS\text{-}H2O}$ is almost 4 times that of $\gamma_{nylon6\text{-}H2O}$. This result is consistent with the onset of non-negligible dimensional swelling in hydrated APS networks. Hydration-dependent swelling produces a strong concentration-dependence of water diffusion through APS networks. Empirical models for perfusion-assisted shape recovery in APS shape-memory microfluidics can be constructed by relating the sorption kinetics with the resulting concentration-dependent modulus. The kinetics of modulus reduction upon hydration are shown in **Figure 8**. The normalized Young's modulus of the APS networks is defined as:

$$\bar{E} = \frac{E(c)}{E_{dry}} \tag{5}$$

where $E(c)$ is the hydration-dependent Young's modulus and E_{dry} is the Young's modulus of the dehydrated APS networks. The normalized Young's modulus of the APS networks decreases

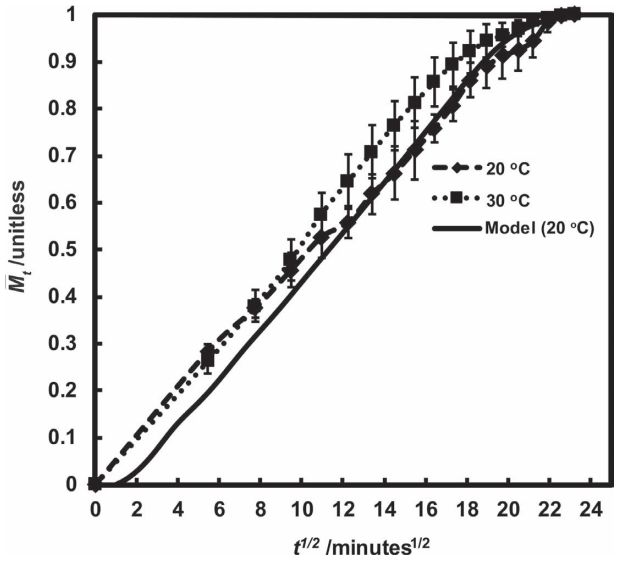

Figure 7. Normalized absorption kinetics curves of water in APS at 20 and 30 °C and modeled absorption kinetics curves of water in APS for 630 ± 50 µm thick samples (n = 4). APS exhibits $\bar{M}_t \propto t^{1/2}$ behavior until late time scales. This data suggests that the diffusion of water in APS networks observes Fickian behavior at both 20 and 30 °C. The modeled curve was derived from time-dependent concentration profiles of APS generated using finite element modeling (FEM). In order to estimate the dependence of D on c and the values of D_o and γ, absorption kinetics curves were generated from FEM concentration profiles by varying D_o and γ over five orders of magnitude. Possible ranges of optimum values of D_o and γ were subsequently narrowed by comparing FEM generated kinetics curves with the experimental absorption kinetics curve and the values of D_o and γ for which the FEM generated concentration curve best fit the experimental curves were extracted. The values of D_o and γ calculated from FEM are 0.033×10^{-8} cm^2 s^{-1} and 0.54 cm^3 mmol^{-1}, respectively.

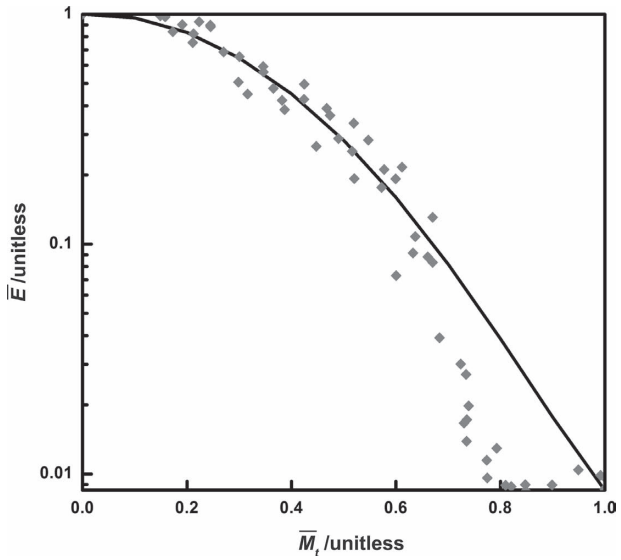

Figure 8. Hydration-dependent Young's modulus ($\bar{E}$) in APS films. A composite of discrete data points from samples (n = 6) are shown as grey diamonds. The line represents a best fit based on the form $\bar{E} = \exp\left(-\sqrt{\frac{(\bar{M}_t - \bar{M}_{off})}{\bar{M}_{char}}}\right) + \bar{E}_o$ where $\bar{M}_{off}$ represents the offset value in hydration (0.014), $\bar{M}_{char}$ represents the characteristic value of hydration for the modulus reduction (0.43) and $\bar{E}_o$ represents the component of the normalized modulus that is independent of $\bar{M}_t$ (0.0030).

until $\overline{M}_t$ 0.8 (Figure 8). The hydration of polyamide networks leads to an exponential reduction in modulus.[48] The decrease in $E(c)$ with c can be predicted using the following relationship:

$$E(c) = E_o \exp\left(-\frac{c}{c_o}\right) \quad (6)$$

where E_o is an initial modulus value when $c = 0$ and c_o is the concentration required to reduce E_o by 36.8% (e^{-1}) (Supporting Information Figure S4).[49] The values of E_o and c_o for water in APS networks are calculated to be 420 MPa and 2.4 mmol cm^{-3}, respectively. The variation of $E(c)$ with c is unique in APS due to the dual-hydration mechanisms of micropore filling and network swelling.

The shape recovery kinetics for the three modes of operation were simulated using finite element modeling (Supporting Information Figures S5, S6, and S7). The simulated and experimental recovery kinetics for all three modes of operation modes are plotted in Figure 5. Although there are notable deviations between the experimental and predicted values for both t_{onset} and t_{50}, the model is able to accurately predict the overall features of $R_r(t)$. This is evident by the closeness of the values of $\int R_r(t)_{exp} dt / \int R_r(t)_{mod} dt$ to unity for both the EXT_{stat} and INT_{perf} modes of operation. Nevertheless, a brief discussion on the origion of the discrepancies in t_{onset} and t_{50} is warranted. For each mode of operation, the model marginally overestimates the t_{onset} (Figure 6). This might be due to accelerated water penetration through porous defects that are formed at the apical surface of APS films. These defects result from the release of water vapor that evolves during thermal curing of polymer films. The model also marginally overestimates t_{50} for both the EXT_{stat} and INT_{perf} modes of operation (Figure 6). The model underestimates t_{50} for the INT_{perf}+EXT_{stat} mode of operation. This deviation can be potentially explained by the presence of a small volume fraction of heterogeneous highly crosslinked domains. The presence of these heterogeneous domains is supported by non-uniform film morphologies after film degradation.[37] The rate of water diffusion through highly crosslinked heterogeneous domains would be significantly slower compared to diffusion through the continuous matrix composed of loosely crosslinked domains. The hydration of loosely crosslinked domains of APS films operating in the INT_{perf}+EXT_{stat} mode is expected to be very rapid. Hence, the rate limiting step in shape recovery for materials in the INT_{perf}+EXT_{stat} operating mode is the diffusion of water into the highly crosslinked domains. This secondary diffusion process ultimately reduces the rate of modulus reduction and therefore increases the shape recovery time line in a manner that is not captured by the model, which assumes homogeneous hydration of uniform APS films. The impact of hydration can influence the mechanism of shape memory recovery in APS films in other facets as well. Shape-memory APS microfluidics achieve incomplete recovery where the strain recovery ratio R_{rvy} is 91 ± 1%. R_{rvy} is defined as:

$$R_{rvy} = \frac{\varepsilon_u - \varepsilon_p}{\varepsilon_u - \varepsilon_o} \times 100 \quad (7)$$

where ε_p is the residual deformed length after complete recovery. Incomplete recovery ($R_{rvy} < 100\%$) can be attributed to dimensional swelling due to hydration of APS networks. Uniform dimensional swelling upon hydration directly counteracts the recovery of polymeric networks that are programmed into temporary geometries by applying tension.

There is a slight discrepancy between the positioning of the microchannels in the experimental shape memory microfluidic devices and the geometry used in the model. This offset is a result of the manual positioning of the films during lamination. While incorporating this spatial artifact does not significantly impact the calculated values for t_{onset} and t_{50} values for the EXT_{stat} and INT_{perf} + EXT_{stat} modes of operation, there is a subtle impact on the INT_{perf} mode (Supporting Information Figure S9). The sensitivity of recovery times with channel spacing was also compared for the three modes of operation by simulating recovery in samples with 700 μm and 1050 μm channel spacing. The recovery times in the INT_{perf} mode of operation exhibit the highest sensitivity to channel spacing (Supporting Information Figure S10). However, increasing the characteristic channel spacing did not significantly impact the calculated values for t_{onset} and t_{50} in the EXT_{stat} mode. The values for t_{onset} and t_{50} in the INT_{perf} + EXT_{stat} exhibit a moderate dependence on microchannel spacing.

3. Conclusions

Reducing the effective macroscopic diffusion length scale in a manner that is analogous to vascularization of tissue structures can accelerate the actuation of stimuli-responsive materials. Here, the utility of this concept has been validated in the design and fabrication of vascularized shape-memory APS polymers. Integrating microvascular networks into bulk materials reduces the characteristic dimensions of the network that govern the time scales for diffusive processes. This ultimately accelerates phase transitions in chemo-responsive SMPs. This strategy enables rapid perfusion-assisted delivery of stimuli into bulk APS networks, which ultimately accelerates the strain recovery kinetics in the SMP. This concept can be extended to other materials to enhance the ability to trigger phase transitions in form factors with large characteristic dimensions. Vascularization of bulk materials is a general strategy that could be further broadened to create next-generation smart materials.

4. Experimental Section

Shape-Memory Polymer Preparation and Device Fabrication: Poly(1,3-diamino-2-propanol-*co*-polyol sebacate) (APS) pre-polymer was synthesized as previous described.[37] Briefly, 1,3-diamino-2-propanol (0.1 mol) (Sigma, St. Louis, MO, USA), glycerol (0.05 mol) (Mallinckrodt chemicals, St. Louis, MO, USA) and sebacic acid (0.15 mol) (Sigma, St. Louis, MO, USA) were condensed in a round bottom flask for 2 h under a N_2 blanket at 130 °C. Melt condensation polymerization was performed at 130 °C and 50 mTorr for 14 h. Replica-molded elastomeric APS films were prepared by curing APS pre-polymer on negative silicon masters that were prepared by photolithography and deep-reactive-ion etching as previously described.[36] The etched silicon mold was cleansed using piranha, solvents, and UV-ozone for 10 min at 90 °C. A sacrificial release layer of maltose (100% w/w) in ddH_2O was spin coated (KW-4A, Chemat scientific, Northridge, CA, USA) at 1500 rpm for 90 s on the etched silicon substrates. Thermoset APS films of 240 μm thicknesses were prepared from pre-polymer films at surface mass densities of 52 mg cm^{-2}. Crosslinked APS films were prepared by curing APS pre-polymer at 180 °C at 50 mTorr for 14 h.

Device Fabrication: Sol-free APS networks were prepared by incubating crosslinked films in ethanol (95%) for 12 h followed by equilibrating in ddH_2O for 12 h. Microfluidic APS networks were prepared by bonding hydrated sol-free films via an additional curing step at 170 °C under 50 mTorr vacuum for 24 h. The fidelity of bonding and replica-molding was verified through scanning electron microscopy (Philips XL-30 FEG, FEI, Hillsboro, OR, USA). Samples were coated with a 3 nm layer of platinum before imaging (Emtech K575X, Quorum Technologies, Guelph, ON, Canada).

Thermomechanical Characterization: Hydrated and dehydrated APS films were prepared into strips for tensile testing (L x W x T = 25 × 10 × 0.5 mm^3, n = 5). Mechanical properties were characterized at 20 °C using a strain rate of 1 mm min^{-1} (Instron 5943 equipped with either a 50 or 500 N load cell, Norwood, MA, USA). Thermomechanical properties of dehydrated APS films were measured using a differential scanning calorimeter with a heating rate of 10 °C min^{-1} (Q-20, TA instruments, New England, DE, USA). The T_g of hydrated APS networks was calculated using the following relationship[50]

$$T_{g1,2} = \frac{T_{g1}(1-x)\Delta C_{p1} + T_{g2}x\Delta C_{p2}}{(1-x)\Delta C_{p1} + x\Delta C_{p2}} \quad (8)$$

where $T_{g1,2}$ is the effective glass transition temperature of the hydrated APS networks, T_{gi} is the glass transition temperature of pure component i, ΔC_{pi} is the change in heat capacity at T_{gi} and x is the mass fraction of component 2. Components 1 and 2 are the APS networks and water, respectively. The mass fraction of water in hydrated APS networks (x) was calculated by measuring the differential mass of APS polymer slabs before M_{dry} and after hydration M_{hyd}.

$$x = \frac{M_{hyd} - M_{dry}}{M_{dry}} \quad (9)$$

APS films (L x W x T = 20 × 10 × 0.50 mm^3, n = 6) were prepared to measure the Young's modulus dependence on hydration. The stress-strain curves of dehydrated APS films were measured at a strain rate of 0.2 mm min^{-1} (Instron 5943 equipped with 50 N load cell, Norwood, MA USA). The samples were then incubated in ddH_2O at 20 °C. The samples were recovered at 10 min intervals and excess water was removed. The stress-strain curves were measured at a strain rate of 0.20 mm min^{-1} after which the samples were returned to water. Individual mechanical measurements were completed in less than 4 min. Dimensions were normalized and were plotted against $\bar{M}_t$ using the folowing relationship:[45]

$$\bar{M}_t = \frac{4}{h}\left(\frac{D_{ave}t}{\pi}\right)^{0.5} \quad (10)$$

where h is the thickness of the samples and D_{ave} is an average diffusion coeffecient. From Equation 3, D_{ave} is calculated to be 2.7×10^{-8} cm^2 s^{-1}.

The strain fixity ratio R_f was calculated by straining APS polymer strips (L x W x T = 13 × 10 × 0.50 mm^3, n = 4) by 10% at 75 °C and cooling the strained APS strips to 20 °C

Hydration Studies: Water sorbtion kinetics in APS networks were measured via gravimetry. Briefly, cylindrical APS samples (n = 4, D = 1.5 cm, H = 630 ± 50 μm) were incubated in ddH_2O at either 20 or 30 °C. The samples were retrieved at preselected time points and excess water was removed. The mass of the samples was recorded and the coupons were immediately reintroduced to the water bath.

Strain Recovery Kinetics: APS films were fabricated into shape-memory microfluidic devices with nominal dimensions (L x W x T) of

$30 \times 6.6 \times 0.82$ mm^3. The temporary shape was induced by heating to 75 °C and applying a ε_m of 11.0 ± 0.3% at a rate of 1 mm min^{-1}. The temporary shape was fixed by cooling the strained APS devices to 20 °C while under applied tension. Strain recovery in microfluidic shape-memory devices was initiated by supplying water at 20 °C as a stimulus agent in three different modes: (1) EXT_{stat}, (2) INT_{perf} and (3) INT_{perf}+EXT_{stat}. All shape-memory recovery experiments were repeated in triplicate. In INT_{perf} operation, ddH_2O (T = 20 °C) was supplied to the APS devices at a volumetric flow rate of 0.01 ml min^{-1} using a syringe pump (KDS-210, Kd Scientific, Holliston, MA, USA) and the recovery at ambient temperature was captured by high-resolution camera (Pro Webcam C910, Logitech, Fremont, CA, USA). In EXT_{stat} operation, the devices were immersed in a water bath at 20 °C while the microchannels remained dry. In INT_{perf}+EXT_{stat} operation, water was flowed through microchannels while the devices were immersed in a water bath held constant at 20 °C. Strain recovery was quantified using NIH ImageJ. All data presented as mean ± standard deviation unless otherwise stated.

Finite Element Modeling: Diffusion of water through APS microfluidic devices functioning in the three different modes of operation was modeled using COMSOL Muliphysics (Version 4.2.0.150, Burlington, MA, USA). The Transport of Dilute Species module was selected to simulate diffusion with corresponding pre-defined concentration dependent diffusion coefficients. The cross-sectional device geometry was constructed and initial boundary concentration values of 11 mmol cm^{-3} and no flux boundary conditions were assigned in accordance with the specific mode of operation. Assigning the triangulation method as an advancing front created a user-defined mesh. Time-dependent solutions were obtained and concentration profiles for discrete time points were generated (Supporting Information Figures S5–7). The relationships between the data extracted from experimental measurements and FEM simulations are summarized in Supporting Information Figure S11. The values of the definite integrals to calculate $\int R_r(t)_{exp} dt / \int R_r(t)_{mod} dt$ were independently determined using the trapezoidal method for both experimental and predicted values for $R_r(t)$ for each operation mode. The range of the definite integral was t = [0, 14] h for both EXT_{stat} and INT_{perf} modes and t = [0, 10] h for the INT_{perf} + EXT_{stat} mode.

Supporting Information

Supporting Information is available from the Wiley Online Library or from the author.

Acknowledgements

Funding provided by the following organizations: the Berkman Foundation; the American Chemical Society Petroleum Research Fund (ACS PRF #51980-DNI7); the Proctor & Gamble Education Grant Program; and the Carnegie Mellon University School of Engineering.

Received: December 6, 2012
Revised: March 17, 2013
Published online: May 6, 2013

[1] M. J. Reiss, *J. Biol. Educ.* **1987**, *21*, 97.
[2] H. H. Hardy, R. E. Collins, R. E. Calvert, *Med. Biol. Eng. Comput.* **1982**, *20*, 550.
[3] L. Loepfe, J. Martinez-Vilalta, J. Piñol, M. Mencuccini, *J. Theor. Biol.* **2007**, *247*, 788.
[4] I. P. Bond, P. M. Weaver, R. S. Trask, H. R. Williams, *J. R. Soc. Interface* **2008**, *5*, 55.
[5] K. S. Toohey, N. R. Sottos, J. A. Lewis, J. S. Moore, S. R. White, *Nat. Mater.* **2007**, *6*, 581.
[6] K. S. Toohey, C. J. Hansen, J. A. Lewis, S. R. White, N. R. Sottos, *Adv. Funct. Mater.* **2009**, *19*, 1399.
[7] C. J. Hansen, S. R. White, N. R. Sottos, J. A. Lewis, *Adv. Funct. Mater.* **2011**, *21*, 4320.
[8] L. D. Zarzar, P. Kim, J. Aizenberg, *Adv. Mater.* **2011**, *23*, 1442.
[9] A. P. Esser-Kahn, P. R. Thakre, H. Dong, J. F. Patrick, V. K. Vlasko-Vlasov, N. R. Sottos, J. S. Moore, S. R. White, *Adv. Mater.* **2011**, *23*, 3654.
[10] L. M. Bellan, S. P. Singh, P. W. Henderson, T. J. Porri, H. G. Craighead, J. A. Spector, *Soft Matter* **2009**, *5*, 1354.
[11] J. T. Borenstein, H. Terai, K. R. King, E. J. Weinberg, M. R. Kaazempur-Mofrad, J. P. Vacanti, *Biomed. Microdevices* **2002**, *4*, 167.
[12] M. Shin, K. Matsuda, O. Ishii, H. Terai, M. Kaazempur-Mofrad, J. T. Borenstein, M. Detmar, J. P. Vacanti, *Biomed. Microdevices* **2004**, *6*, 269.
[13] M. Cabodi, N. W. Choi, J. P. Gleghorn, C. S. D. Lee, L. J. Bonassar, A. D. Stroock, *J. Am. Chem. Soc.* **2005**, *127*, 13788.
[14] S. C. Olugebefola, A. M. Aragon, C. J. Hansen, A. R. Hamilton, B. D. Kozola, W. Wu, P. H. Geubelle, J. A. Lewis, N. R. Sottos, S. R. White, *J. Compos. Mater.* **2010**, *44*, 2587.
[15] J. A. Lewis, *Adv. Funct. Mater.* **2006**, *16*, 2193.
[16] S. A. Soper, S. M. Ford, S. Qi, R. L. McCarley, K. Kelly, M. C. Murphy, *Anal. Chem.* **2000**, *72*, 642.
[17] L. M. Bellan, M. Pearsall, D. M. Cropek, R. Langer, *Adv. Mater.* **2012**, *24*, 5187.
[18] N. W. Choi, M. Cabodi, B. Held, J. P. Gleghorn, L. J. Bonassar, A. D. Stroock, *Nat. Mater.* **2007**, *6*, 908.
[19] D. T. Nguyen, Y. T. Leho, A. P. Esser-Kahn, *Adv. Funct. Mater.* **2013**, *23*, 100.
[20] J. H. Huang, J. Kim, N. Agrawal, A. P. Sudarsan, J. E. Maxim, A. Jayaraman, V. M. Ugaz, *Adv. Mater.* **2009**, *21*, 3567.
[21] S. K. Sia, B. M. Gillette, G. J. Yang, *Birth Defects Res. C* **2007**, *81*, 354.
[22] A. D. Van der Meer, A. A. Poot, M. H. G. Duits, J. Feijen, I. Vermes, *J. Biomed. Biotechnol.* **2009**, *2009*, 823148.
[23] G. Y. Huang, L. H. Zhou, Q. C. Zhang, Y. M. Chen, W. Sun, F. Xu, T. J. Lu, *Biofabrication* **2011**, *3*, 012001.
[24] C. Fidkowski, M. R. Kaazempur-Mofrad, J. Borenstein, J. P. Vacanti, R. Langer, Y. Wang, *Tissue Eng.* **2005**, *11*, 302.
[25] Y. Du, C. Donald, M. R. K. Mofrad, J. E. Weinberg, A. Khademhosseini, J. T. Borenstein, in *Microfluidics for Biological Applications* (Eds: W.-C. Tian, E. Finehout), Springer, Berlin- Heidelberg, Germany **2009**, p. 223.
[26] P. T. Mather, X. Luo, I. A. Rousseau, *Annu. Rev. Mater. Res.* **2009**, *39*, 445.
[27] M. Behl, A. Lendlein, *Mater. Today* **2007**, *10*, 20.
[28] A. Lendlein, S. Kelch, *Angew. Chem. Int. Ed.* **2002**, *41*, 2034.
[29] M. A. Ward, T. K. Georgiou, *Polymers* **2011**, *3*, 1215.
[30] J. Merline, C. Nair, *J. Appl. Polym. Sci.* **2008**, *107*, 4082.
[31] X. K. Lin, L. Chen, Y. P. Zhao, Z. Z. Dong, *J. Mater. Sci.* **2010**, *45*, 2703.
[32] H. Du, J. Zhang, *Soft Matter* **2010**, *6*, 3370.
[33] B. Yang, W. M. Huang, C. Li, C. M. Lee, L. Li, *Smart Mater. Struct.* **2004**, *13*, 191.
[34] S. Chen, J. Hu, C. Yuen, L. Chan, *Polymer* **2009**, *50*, 4424.
[35] S. L. Simkevitz, H. E. Naguib, *High Perform. Polym.* **2009**, *22*, 159.
[36] J. Wang, C. J. Bettinger, R. S. Langer, *Organogenesis* **2010**, *6*, 212.
[37] C. J. Bettinger, J. P. Bruggeman, J. T. Borenstein, R. S. Langer, *Biomaterials* **2008**, *29*, 2315.

[38] C. J. Bettinger, E. J. Weinberg, K. M. Kulig, J. P. Vacanti, Y. Wang, J. T. Borenstein, R. Langer, *Adv. Mater.* **2006**, *18*, 165.
[39] F. A. Long, L. J. Thompson, *J. Polym. Sci.* **1955**, *15*, 413.
[40] H. Hopfenberg, L. Nicolais, E. Drioli, *Polymer* **1976**, *17*, 195.
[41] T. Alfrey Jr, E. F. Gurnee, W. G. Lloyd, *J. Polym. Sci., Part C: Polym. Lett.* **1966**, *261*, 249.
[42] M. A. Del Nobile, G. Mensitieri, P. A. Netti, L. Nicolais, *Chem. Eng. Sci.* **1994**, *49*, 633.
[43] H. Frisch, *Polym. Eng. Sci.* **1980**, *20*, 2.
[44] S. Prager, F. Long, *J. Am. Chem. Soc.* **1951**, *73*, 4072.
[45] N. R. Manoj, D. Ratna, R. A. Weiss, *Macromol. Res.* **2004**, *12*, 26.
[46] H. Fujita, *Fortschr. Hochpolym.-Forsch.* **1961**, *3*, 1.
[47] S. Marais, Q. T. Nguyen, C. Devallencourt, M. Metayer, T. U. Nguyen, P. Schaetzel, *J. Polym. Sci. Part B: Polym. Phys.* **2000**, *38*, 1998.
[48] K. Inoue, S. Hoshino, *J. Polym. Sci. Polym. Phys.* **1976**, *14*, 1513.
[49] H. Reimschuessel, *J. Polym. Sci. Polym. Chem.* **1978**, *16*, 1229.
[50] P. R. Couchman, F. E. Karasz, *Macromolecules* **1978**, *11*, 117.